Sensors and Materials, Vol. 36, No. 4 (2024) 1693–1706
MYU Tokyo

S & M 3627

Employment of Finite Element Analysis Method to Analyze the Thermal Effects of Direct Energy Deposition on SUS316L

Wenjie Zheng,[1] Hung-Yu Chang,[2] Chao-Ming Hsu,[2*] and Cheng-Fu Yang[3,4**]

[1]School of Ocean Information Engineering, Jimei University, Xiamen 361021, Fujian, China
[2]Department of Mechanical Engineering, National Kaohsiung University of Science and Technology, Kaohsiung 807, Taiwan
[3]Department of Chemical and Materials Engineering, National University of Kaohsiung, Kaohsiung 811, Taiwan;
[4]Department of Aeronautical Engineering, Chaoyang University of Technology, Taichung 413, Taiwan

(Received January 3, 2024; accepted April 17, 2024)

Keywords: direct energy deposition, finite element method, ANSYS, displacement, SUS316L

In this study, we investigated the displacement behavior of SUS316L stainless steel under five consecutive direct energy depositions through experiments and the use of the ANSYS commercial finite element method software. We explored the effects of displacement after cooling the five deposited layers and examined the relationship between different curvatures and laser parameters, including laser power and laser feed rate. In this research, a complete cross-sectional profile was obtained through experiments. Subsequently, simulations were conducted using laser powers of 300, 400, and 500 W, along with laser feed rates of 3, 5, and 7 mm/s, employing a thermal-solid coupling model. The results indicated that the optimal preheating temperature during the deposition process was around 150 °C, leading to a more stable displacement difference. The influence of curvature on displacement was relatively consistent along the neutral axis, allowing for the prediction of large displacement amounts along a straight-line path. Through simulation, it could be understood that when utilizing direct energy deposition to deposit SUS316L, considering the displacement conditions during the deposition process, it was preferable to use a low laser power and a high deposition rate.

1. Introduction

Wohlers Associates conducts long-term investigations into the overall market value of additive manufacturing, as well as relevant research. The global additive manufacturing market exhibited a compound annual growth rate (CAGR) of over 17% from 2012 to 2017, according to their findings. Sales figures for related products and services also showed consistent yearly growth, reaching $7.336 billion in 2017, with the number of machines sold reaching 528952.[(1)] Numerous companies worldwide have purchased related equipment for additive manufacturing and engaged in research and development. They have incorporated additive manufacturing technology into their processes to reduce associated costs and save manpower. Additive manufacturing has expanded into various industries, including electronics, commerce,

*Corresponding author: e-mail: jammy@nkust.edu.tw
**Corresponding author: e-mail: cfyang@nuk.edu.tw
https://doi.org/10.18494/SAM4892

ISSN 0914-4935
https://myukk.org/

automotive, aerospace, biomedicine, and military industries. The largest application market is in commercial machines, accounting for 17.5% of the overall market, followed by electronic products at 16.6%. It is anticipated that the overall market for the additive manufacturing industry will reach $35.6 billion by the year 2024.

With the advancement of technology, mechanical components are becoming increasingly complex. While the emergence of five-axis machine tools in traditional machining has reduced the setup time to some extent, the overall processing time remains excessively long, and the shaping is still constrained. In additive manufacturing (AM), unlike traditional subtractive manufacturing in machining, a stacking manufacturing approach is adopted to avoid material waste.[2] Direct energy deposition is also known as laser metal deposition (LMD).[3] In the forming process of direct energy deposition, there are interactions among laser light, the powder, and the substrate. During the injection of powder into the molten pool, the powder undergoes a transition from a solid to a liquid state owing to the high-density and intense energy absorption of the laser beam. Simultaneously, the powder causes attenuation of the light particles and directs the attenuated laser light onto the substrate. On the substrate, only a portion of the attenuated laser light is absorbed, heating the substrate to create a molten pool. The melted powder can then be deposited and mixed onto the substrate molten pool before solidification.

In the past, two distinct methods were employed to assess the thermal effects of direct energy deposition on the growth of SUS316L. The first method involved the utilization of various sensors affixed to the deposited SUS316L. For instance, Smoqi *et al.* implemented in-process sensor-based monitoring and closed-loop control to alleviate the adverse impacts of flaw formation and microstructure heterogeneity in the directed energy deposition process.[4] Another approach was taken by Nunez *et al.*, who employed two different configurations (exposed and embedded tips) and two designs to integrate type K thermocouples into 316L stainless-steel samples. In one design, the sensor was positioned directly onto the substrate, flush with it, while the second design involved the use of an additive manufacturing base.[5] Additionally, employing thermal modeling for the directed energy deposition of a composite coating is not only highly efficient but also a valid approach for understanding the deposition process in terms of various parameters. This method proves advantageous as researchers can simulate the process without the need for a substantial financial investment in the actual deposition of SUS316L. By utilizing simulation techniques, significant cost savings can be achieved while still gaining valuable insights into the intricate details of the deposition process and its response to different parameters.[6,7]

In this paper, we used AutoCAD and SolidWorks to create the models, and after completing the preprocessing stage, we imported the models into ANSYS for meshing and computational analysis. The modules we employed included the transient heat conduction module and the transient solid force module. The simulated deposition model in this study was primarily divided into two main parts. First, inspired by the concept that the substrate and powder are correlated, as proposed by Yan,[8] the idea that the deposition and substrate have a similar relationship is developed. This concept is based on the research method of buckling deformation and validates the experimental findings of buckling deformation.[9] The substrate was designed to be a thin and elongated shape with the dimensions of 200 × 50 × 1 mm^3, and a deposition of a 25-mm-

thick layer was performed in the middle of the substrate, using a SUS316L steel plate and the morphology of a single-layer real deposit. Second, a numerical analysis model was developed for the multilayer deposition of the deposit. As the thickness of the substrate increased, the deformation of the substrate was converted into stress on the deposit. Therefore, a substrate thickness of 20 mm was chosen, with its length and width set to 60 mm, consistent with the experimental deposition conditions. The objective of this approach was to investigate the correlation between the substrate characteristics and the resulting deposition, with a particular focus on the structural appearance transformation caused by substrate deformation during the deposition process. The main methodology involved utilizing finite element simulation software to establish a model that integrated experimental validation and numerical analyses, providing a comprehensive understanding of the deposition behavior in the proposed simulation framework.

2. Simulation Process and Parameters Used

Regarding the establishment of the finite element analysis conditions, in the process of direct energy deposition, the process of direct energy deposition is influenced by multiple factors such as the laser power, spot diameter, deposition rate, and movement path. These factors may induce thermal stress and displacement, thereby affecting the precision and surface roughness of components, leading to uncertainties. To avoid defect generation, in this study, we primarily explore the possible displacement shapes and postdeposition deformation under various laser powers, spot diameters, deposition rates, and movement paths during direct energy deposition. Since direct energy deposition is similar to welding principles and involves multiple physical phenomena, a significant amount of computational resources and time is required for finite element analysis.[10] Therefore, to effectively save analysis time and enhance numerical convergence, in this study, we have simplified the conditions and assumed the following conditions.

1. The coating material and substrate material are both SUS316L, and they exhibit mutually influencing characteristics.[8]
2. Residual stresses are induced by thermal effects. Without considering metal liquid flow or phase changes, the model is simplified into a thermal-stress coupling analysis mode.[11,12]
3. Because of the rapid heating and cooling nature of direct energy deposition under laser irradiation, thermal losses caused by radiation are negligible and are not considered within the scope of this study.[13]
4. The space is an open environment with natural convection.

The simulation modules were capable of directly addressing the energy deposition process in highly transient nonlinear problems, enabling corresponding analyses. The density of the Stainless-Steel 316 series (SUS316L) at room temperature is approximately 8000 kg/m^3, the thermal conductivity is about 13 W/m°C, the specific heat is around 498.73 J/kg°C, Young's modulus is approximately 195 GPa, and the melting point is 1350 °C. In this paper, the variations of density, thermal conductivity, specific heat, and Young's modulus with temperature will be depicted as shown in Fig. 1. However, in finite element analysis, when conducting thermal stress calculations, parameters that are not set beyond the melting point will be directly assigned the

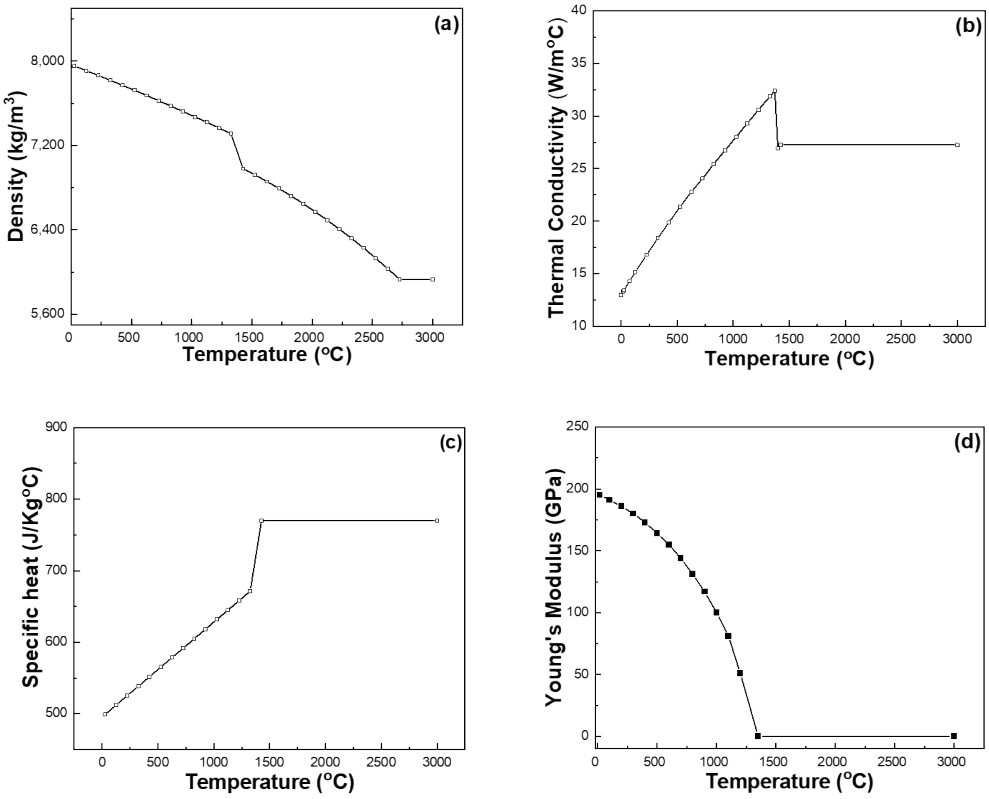

Fig. 1. Material properties of SUS316L with temperature variation: (a) density, (b) thermal conductivity, (c) specific heat capacity, and (d) Young's modulus.

values from the preceding temperature. Since the material undergoes a phase transition from solid to liquid above the melting point, setting Young's modulus to exactly 0 could lead to computational divergence. Therefore, after the melting point, Young's modulus is set to approach a value close to 0 for proper calculation.

Here, we outline the overall modeling process of cross-sectional morphology obtained through experimentation. The substrate and powder used were SUS316L, and the specimen was a 30 × 40 × 20 mm^3 rectangular prism. Inert gas argon was used for both powder and protective gases, with injection velocities of 4 and 6 mm^2/s, respectively, and a powder feed rate of 3.495 g/min. The initial laser spot diameter was 1.2 mm, with a nozzle-to-substrate distance of 10 mm. The *Z*-axis displacement of the nozzle for each layer was referenced to Table 1. The deposition path followed a reciprocating pattern, with each layer deposited to a length of 20 mm. After deposition, traditional machining methods were avoided to prevent morphological distortion. Instead, a wire electrical discharge machining (EDM) machine, which minimally impacts the overall appearance, was chosen for specimen processing. After processing, optical microscopy was used for imaging. The cross-sectional morphology with an error value within 0.01 mm was obtained using a scale and imported into AutoCAD for contouring each layer. The cross-sectional morphologies of one to five layers were overlaid, considering heat dissipation without

Table 1
Layer elevation for cross-sectional morphology experiment under different power (W), ΔZ : lifting amount per layer.

Speed (mm/s)	300 W	400 W	500 W
3	$\Delta Z = 0.5$	$\Delta Z = 0.5$	$\Delta Z = 0.5$
5	$\Delta Z = 0.3$	$\Delta Z = 0.3$	$\Delta Z = 0.3$
7	$\Delta Z = 0.2$	$\Delta Z = 0.2$	$\Delta Z = 0.2$

considering the influence of the molten pool. The planar model was imported into SolidWorks for the creation of a three-dimensional model, and finally exported to ANSYS Workbench for mesh segmentation.

The mesh division for preprocessing was performed using the built-in meshing tool in ANSYS, employing hexahedral elements. In the experimental validation model, the mesh size for the substrate was set at 0.1 mm, while the mesh for the deposited material was determined on the basis of convergence analysis, as illustrated in Fig. 2. For the numerical analysis model, the mesh size for the deposited material was set at 0.1 mm, and the mesh for the substrate became progressively finer as it approached the center of the deposited material.

3. Simulation Results and Discussion

In this study, we delved into the impact of interactions among the substrate, powder, and laser on the deposition process. Previous research has already highlighted the pivotal roles played by the powder and laser in shaping deposited materials, and our experimental results further corroborate this assertion.[8] Specifically, we posited a mutual influence between the substrate and the deposited material, suggesting that such interactions could yield complex effects on morphology formation and final material properties. During processes resembling welding, we observed the more common occurrences of saddle-type buckling and torsional buckling in plate materials. However, it is noteworthy that in our experiment, owing to the smaller width of the deposited plates, the primary deformation manifested as saddle-type buckling, as depicted in Fig. 3. The specificity of this deformation may be influenced by the interactions between the substrate and laser during the deposition process, thereby emphasizing the regulatory role of different parameters in determining deformation modes during deposition.

In conjunction with simulated experiments, we have conducted actual deposition experiments using a 1-mm-thick SUS316L steel plate specimen for direct energy deposition. The clamping method involved fixing the specimen on the left side and depositing material in the middle. During deposition at laser powers of 500 and 400 W, the thin plate experienced melting, resulting in material failure that could not support the weight of the overhanging end, leading to sinking. Therefore, a laser power of 300 W and a laser feed rate of 5 mm/s were employed for direct energy deposition. After the deposition process, the specimen was allowed to cool to room temperature. The observed deformation conditions postcooling aligned with the results obtained from numerical simulations, as shown in Figs. 4 and 5. The use of a lower laser power and optimized feed rate allowed for successful deposition without the detrimental effects observed with higher laser powers. This suggests that the selected parameters strike a balance between

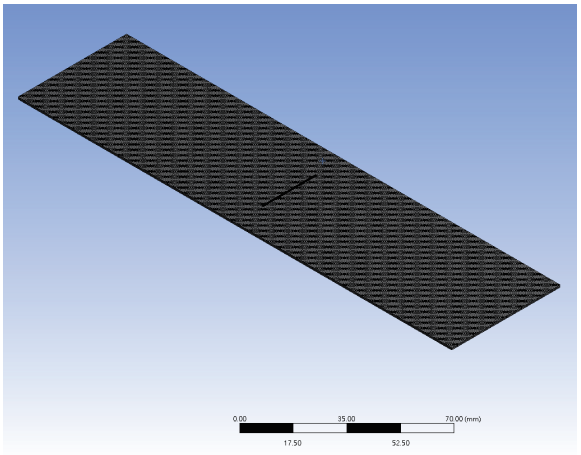

Fig. 2. (Color online) Mesh generation for experimental validation.

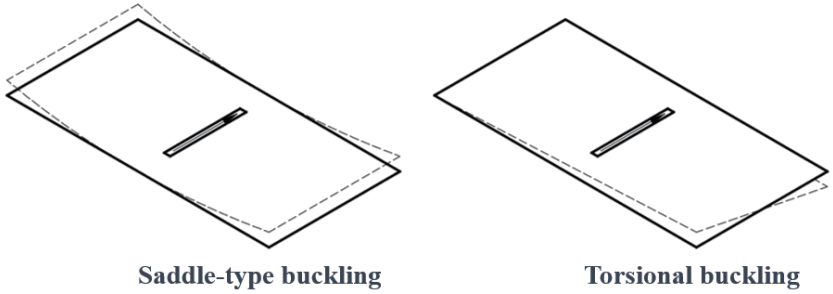

Fig. 3. Deformation patterns in direct energy deposition of thin and long components.

Fig. 4. (Color online) Deformation condition after direct energy deposition.

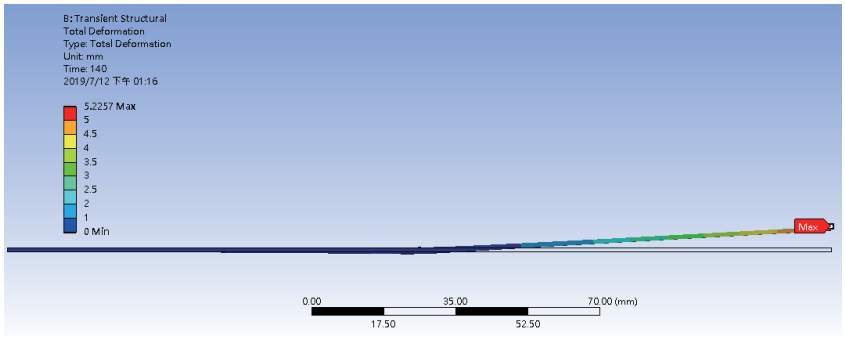

Fig. 5. (Color online) Numerical simulation of deformation.

achieving proper material fusion and avoiding excessive melting, contributing to a more stable and controllable deposition process. The correlation between experimental and simulated deformation further validates the effectiveness of the chosen parameters in maintaining structural integrity during direct energy deposition.

After numerical analysis, the calculated deflection was 5.22 mm, while the experimental measurement yielded a value of approximately 6.20 mm, resulting in a difference of about 1 mm. In the numerical analysis of the direct energy deposition process, and in this study, we did not consider the influence of the flow field and powder delivery. As a result, there were discrepancies in the numerical analysis owing to errors introduced by the forced convection of the protective gas and powder coverage. However, despite these variations, the actual results from the direct energy deposition in this study showed a consistent trend with the ANSYS simulation results, with an error of approximately 16%. Therefore, the finite element method simulation results are in line with the real-world scenario. After validating the method with experimental results, finite element analysis was conducted on the basis of the actual deposition outcomes. Subsequently, displacement analysis was performed under the conditions of a laser power of 300 W and feed rate of 5 mm/s, considering five layers of deposition.

3.1 Displacement analysis in actual direct energy deposition

In further discussion of the results of this study, our focus centers on the numerical simulation of thermal effects and the consistency observed in the experiments. From the simulated results in Fig. 6, it is evident that during the direct energy deposition process, the SUS316L material undergoes elongation and changes over time. The heating heat source moves at different time points and has a notably smaller size during the initial heating stage, as shown in Fig. 6(a).

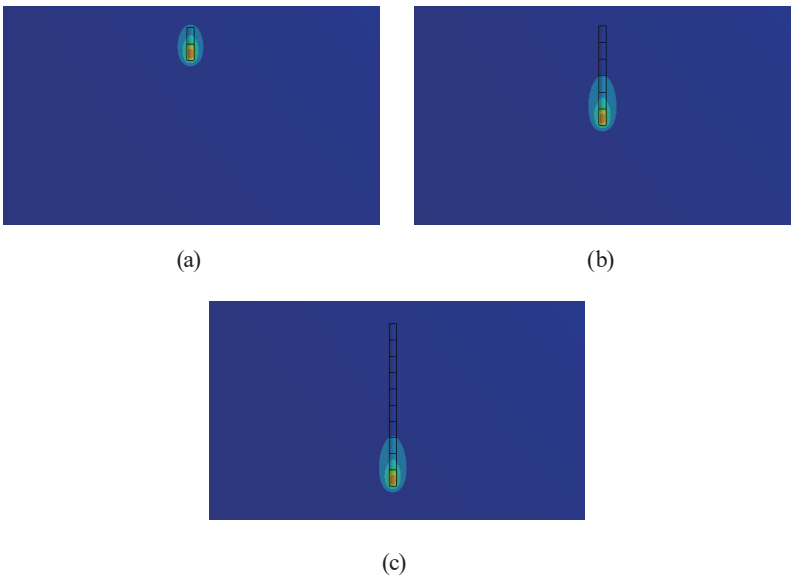

Fig. 6. (Color online) Temperature field variations during the first layer deposition: changes within (a) 1, (b) 3, and (c) 5 s.

However, once the heat source stabilizes, its shape variation becomes minimal, as illustrated in Figs. 6(b)–6(c). During the deposition process, the simulated temperature field indicates that the material's temperature consistently exceeds the melting point of 1350 °C, in agreement with observations in the actual deposition process. This confirms the effectiveness of the parameters and model used in the simulation in capturing the thermal behavior of SUS316L during direct energy deposition. It further underscores the importance of the simulation method in understanding temperature field variations during the deposition process.

In Fig. 7, beyond the simulated temperature field, we also observe displacements at different positions (points a, b, and c) during the simulation. These displacements reflect the strain in the material caused by temperature field variations during the deposition process. These numerical results contribute to a deeper understanding of deformation and stress distribution during the deposition process. In conclusion, the finite element analysis results in this study are consistent with observations from actual experiments, reinforcing the reliability of the simulation method employed. These findings provide valuable insights for future optimizations of the direct energy deposition process, aiming for a more stable and controlled material deposition.

To further explore the temperature field variations and the impact of residual stresses in the experiment, as shown in Fig. 7, we conducted simulations specifically around the stabilized state near the central point b of the deposition path. Displacement measurements were taken at the central point, and measurements at the outermost point a, topmost point b, and innermost point c were conducted near the stabilized deposition path. This design allowed us to gain a more comprehensive understanding of the thermal effects and deformation behavior at different positions during the deposition process. After completing the deposition, we identified the location of the maximum residual stress, which is crucial for the structural integrity of the material. Figure 8 illustrates the temporal changes at the central point b of each layer's deposition path. It was observed that when the heat source arrived, the temperature rapidly rose above the melting point and quickly cooled upon its departure. Such rapid heating and cooling processes may induce changes in the material's microstructure, thereby influencing its mechanical properties.

Subsequently, during the deposition of lower layers, the temperature rose again. This could be related to the accumulation and distribution of energy in the material during the deposition

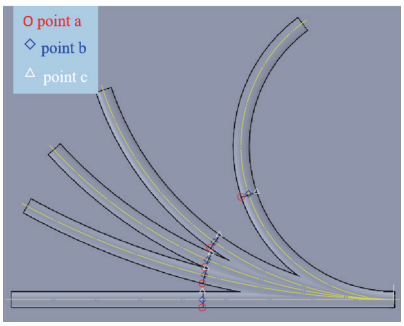

Fig. 7. (Color online) Schematic diagram of measurement points for each layer under multiple curvatures.

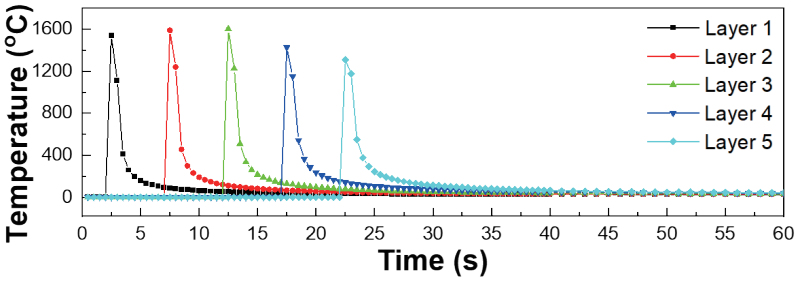

Fig. 8. (Color online) Temporal temperature changes at point b, the center of each layer's deposition path.

process. As the temperature did not return to room temperature after the deposition of each layer, there was a gradual increase in temperature after each deposition cycle. This persistent temperature rise may have lasting effects on the thermal history and structure of the deposited material. In Fig. 9, we observed that the temperature difference between layers gradually decreased over time, reaching a minimum of 8.15 °C in the fifth layer, corresponding to a temperature of approximately 150 °C. This suggests that with an increasing number of deposition layers, the heat source becomes more effectively applied to the deposition process, indicating a potential gradual stabilization of thermal effects.

From the temperature field determined at the measurement points, as shown in Fig. 10, it can be observed that the displacement of each layer just before deposition increases with each layer during the deposition process. Figure 10(a) shows the displacement of measurement points after the completion of the first layer deposition, Fig. 10(b) shows the displacement of measurement points after the completion of the third layer deposition, and Fig. 10(c) shows the displacement of measurement points after the completion of the fifth layer deposition and subsequent cooling. Because of the incomplete cooling at this stage, the deformations have not yet shrunk to the final postcooling dimensions. The displacement values for each layer are as follows: 0.013 mm for the first layer, 0.021 mm for the second layer, 0.027 mm for the third layer, 0.034 mm for the fourth layer, and 0.035 mm for the fifth layer. After cooling-induced contraction, the overall displacement returns to 0.016 mm.

On comparing the above results with the temperature field variations discussed in the previous section, it is evident that the displacement behavior corresponds to the temperature differences. During the deposition process, the temperature differences gradually become smoother, and the displacement values decrease accordingly. In the case of preheating the SUS316L to 150 °C before deposition, the influence of temperature differences on each layer is smaller, resulting in a more stable displacement. Moving on to Fig. 11, each peak corresponds to the moment of completion of deposition and aligns with the temperature field. Before the next deposition, the displacement values do not return to the predeposition values. Approximately 15 s after deposition completion, the displacement shows minimal further change. Compared with Fig. 8, at this point, the cooling stage has approached 65 °C, and heat exchange with the surrounding environment, including gradual thermal convection with room temperature, is occurring.

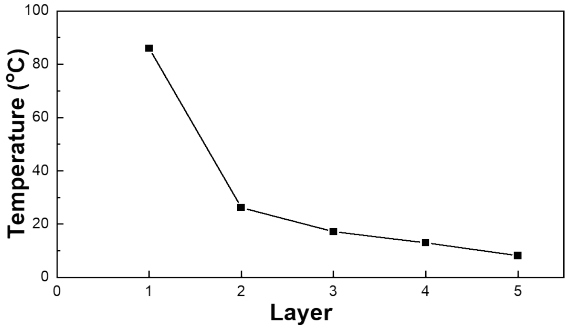

Fig. 9. Temperature difference between each layer and the preceding layer during the stacking process.

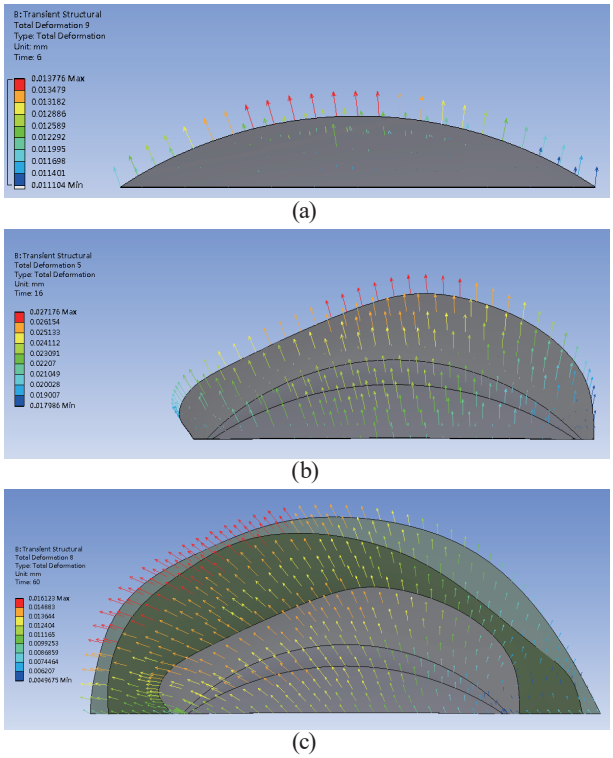

Fig. 10. (Color online) Displacement variation diagrams. Displacement of measurement points after the completion of (a) the first layer deposition, (b) the third layer deposition, and (c) the fifth layer and subsequent cooling.

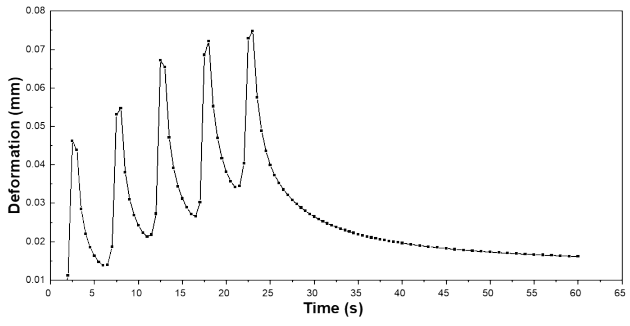

Fig. 11. Displacement variations of measurement points as a function of time.

3.2 Comparison of the effects of stack deposition curvature radius

In this section, we will compare the effects of stack deposition curvature radius. The curvature radius plays a crucial role in determining the characteristics of the deposition process and its outcomes. Figure 12 provides a visual representation of the displacement values for each layer just before deposition, showcasing the variations in displacement across different curvature radii. Observing the results, it is evident that the displacement behavior corresponds to the curvature radius during the deposition process. Each layer's displacement increases with the curvature radius, reaching different magnitudes before the final cooling-induced contraction. Specifically, the displacement values for the first through fifth layers are 0.013, 0.021, 0.027, 0.034, and 0.035 mm, respectively. By examining the temperature field variations discussed in the preceding section, we can discern a gradual smoothing of temperature differences during deposition, accompanied by a proportional reduction in displacement values. Notably, preheating the SUS316L to 150 °C prior to deposition results in a diminished influence of temperature differences on each layer, leading to a more stable displacement. In Fig. 11, each peak aligns with the completion of deposition, demonstrating that the deposition-induced displacement does not fully revert to predeposition values before the subsequent deposition. Approximately 15 s after deposition completion, the displacement stabilizes, coinciding with the cooling stage where the temperature approaches 65 °C and thermal exchange with the environment occurs, including gradual thermal convection at room temperature.

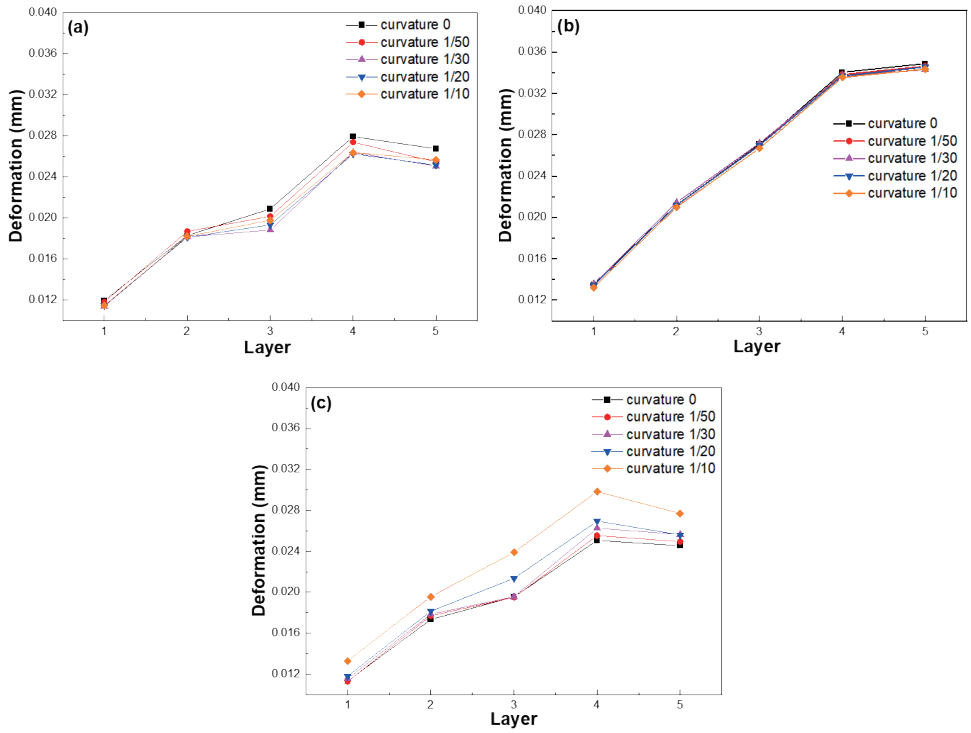

Fig. 12. (Color online) Variation in deposition curvature radii at (a) point a, (b) point b, and (c) point c.

In the preceding section, the results revealed that the maximum displacement behavior during the deposition process occurs in the upper region. However, considering the asymmetry between the inner and outer circles and the neutral axis on the cross section, the relationship between thermal expansion and contraction may lead to different outcomes. In this section, we examine the influence of curvature variation on various parameters during the deposition process. Measurements and comparisons were conducted with a laser power of 300 W and a deposition rate of 5 mm/s, varying the curvature from the deposition's highest point (point a) to the left and right ends of the cross section (points b and c). Figure 12(a) illustrates that, as the curvature decreases, the displacement at the inner circle measurement position (point a) increases. This is attributed to the increased outward heat dissipation area for each layer. On the other hand, as shown in Fig. 12(b), the variation in curvature has minimal impact on the displacement at the top measurement point (point b). Regarding the outer circle's influence, as depicted in Fig. 12(c), a decrease in curvature results in a reduction in displacement owing to the decreased outward heat dissipation area. Understanding the nuanced impact of curvature on displacement at different locations is crucial for optimizing the deposition process and achieving the desired outcomes in additive manufacturing. Further investigation into these effects can guide the refinement of process parameters for enhanced control and performance.

3.3 Displacement analyses of the effects of laser power and scanning rate

Laser power stands as a pivotal parameter influencing the volume of powder deposition, thereby indirectly impacting the deposition height. Endeavors to reduce processing time while simultaneously enhancing deposition height often involve elevating both power and feed rates to improve coating quality. Consequently, investigating the influences of the laser power and feed rate on displacement during the deposition process is a meaningful pursuit. To delve into this, we conducted a comparison of laser power at a deposition speed of 5 mm/s along a linear path, varying the laser power as 300, 400, and 500 W, as depicted in Figs. 13(a)–13(c). Examining Fig. 13 reveals a clear trend: a higher laser power results in a larger deposited volume. Simultaneously, the natural convection area increases, leading to a proportional augmentation in displacement. Notably, points a and c exhibit a trend of curve development, suggesting interactions between power, feed rate, and displacement. In contrast, point b displays a predictable linear progression in displacement for each layer. A strategic consideration is evident: to minimize the cumulative displacement for each layer, deposition at the laser power of 300 W proves optimal. This analysis underscores the importance of a balanced approach in optimizing power and feed rate to achieve efficient powder deposition processes.

Furthermore, we conducted depositions along a linear path with a laser power of 300 W and compared the outcomes of using deposition speeds of 3, 5, and 7 mm/s, as illustrated in Figs. 14(a)–14(c). Figure 14 shows that a notable trend emerges: higher deposition speeds result in smaller deposited volumes. Simultaneously, the reduced natural convection area leads to a decrease in displacement. Notably, for measurements at the highest point, b, the displacements at deposition speeds of 3 and 5 mm/s are similar, with a noticeable decrease observed only at 7 mm/s. On the sides, measuring points a and c exhibit comparable displacements at deposition

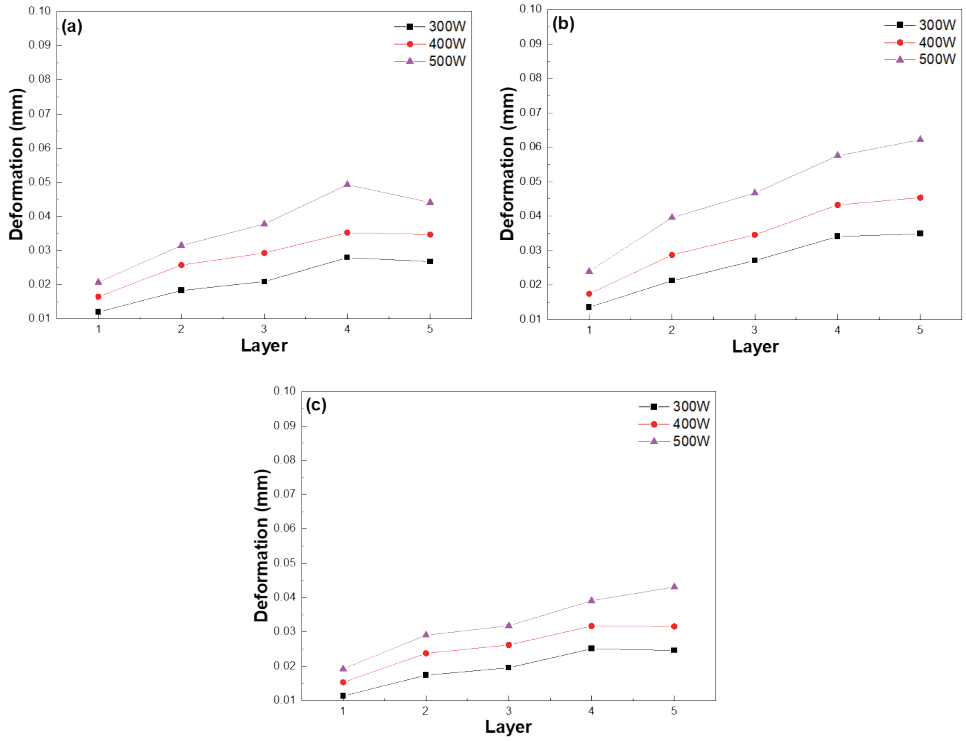

Fig. 13. (Color online) Effects of laser power on deformation at (a) point a, (b) point b, and (c) point c.

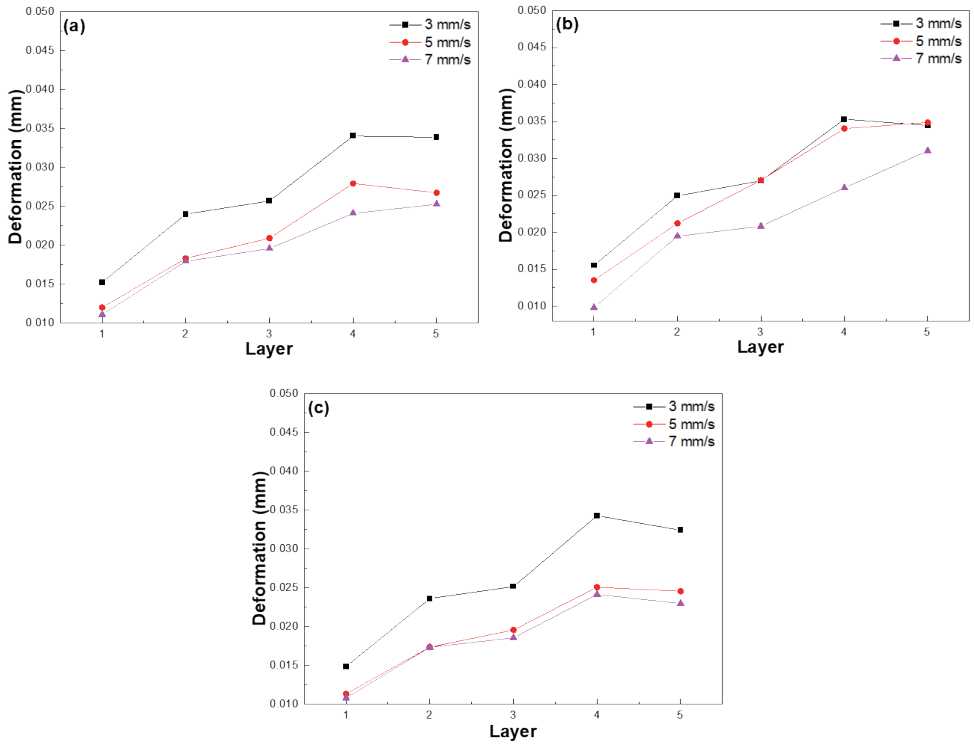

Fig. 14. (Color online) Effects of stack scanning rate on deformation at (a) point a, (b) point b, and (c) point c.

speeds of 5 and 7 mm/s. However, for optimal results and to minimize the cumulative displacement for each layer, deposition at a speed of 7 mm/s is recommended. This examination sheds light on the intricate relationship between deposition speed, displacement, and overall powder deposition quality. Achieving an optimal balance between these parameters is essential for enhancing the efficiency and precision of the deposition process.

4. Conclusions

By utilizing finite element method numerical simulations, parameter adjustments can be made to address displacement effects during the deposition process, with the aim of improving formative heights. In this study, we subjected the direct energy deposition of SUS316L to finite element analysis using the commercial software ANSYS Workbench. The analysis yielded the following conclusions.

1. The optimal preheating temperature during the deposition process is approximately 150 °C.
2. Curvature has a relatively consistent impact on displacement along the neutral axis. Predictions for the z-axis direction can be made using a linear path, with larger influences observed at the periphery and smaller influences at the inner circle. Consideration of deformation issues in both inner and outer circles requires that attention be paid to this aspect.
3. Control over parameters is crucial during the deposition process. To minimize displacement, it is advisable to increase deposition speed and decrease power wattage.

Acknowledgments

This research was supported by the education department of Fujian Province through grant No. JAT210232, Summit-Tech Resource Corp., and projects under Nos. MOST 111-2221-E-390-018 and NSTC 112-2622-E-390-002.

References

1 Wohlers Report 2013–2019 Press Release, https://wohlersassociates.com/product/wr2023/ (accessed October 2019)
2 D. D'Andrea: Metals **13** (2023) 1370.
3 V. Vinoth, T. Sekar, and M. Kumaran: J. Mater. Eng. Perform. **32** (2023) 4138.
4 Z. Smoqi, B. D. Bevans, A. Gaikwad, J. Craig, A. Abul-Haj, B. Roeder, B. Macy, J. E. Shield, and P. Rao: Mater. Design **215** (2022) 110508.
5 L. Nuñez III, P. Sabharwall, and I. J. van Rooyen: Int. J. Adv. Manuf. Technol. **127** (2023) 3611.
6 S. Fetni, T. M. Enrici, T. Niccolini, H. S. Tran, O. Dedry, L. Duchêne, A. Mertens, and A. M. Habraken: Mater. Design **204** (2021) 109661
7 R. Ghanavati, H. Naffakh-Moosavy, M. Moradi, and M. Eshraghi: Sci. Rep. **12** (2022) 16600.
8 J. Y. Yan: Optimal Design of Process, Parameters during Laser Direct Metal Deposition of Multi-Material Parts, Thesis of Ph. D., Clemson University, December, 2016.
9 C. L. Kung, C. K. Hung, C. M. Hsu, and C. Y. Chen: Appl. Sci. **7** (2017) 982.
10 M. Cross, T. Croft, A. Slone, A. Williams, N. Christakis, M. Patel, C. Bailey, and K. Pericleous: 2007. Int. J. Comput. Methods Eng. Sci. **8** (207) 63.
11 A. Plati, J. C. Tan, I. O. Golosnoy, R. Persoons, K. V. Acker, and T. W. Clyne: Adv. Eng. Mater. **8** (20067) 619.
12 P. Loucas, H. Tobias, and F. Z. Michael: J. Laser Appl. **19** (2007) 189.
13 S. Kumar and S. Roy: J. Mechanic. Eng. Sci. **218** (2004) 703.